A Numerical Study on a Mesoscale Convective System over a Subtropical Island with 4D-Var Assimilation of GPS Slant Total Delays

Takuya KAWABATA, Yoshinori SHOJI, Hiromu SEKO, and Kazuo SAITO

Meteorological Research Institute, Japan Meteorological Agency, Tsukuba, Japan

Abstract

A method to assimilate slant total delays derived from global positioning system (GPS) data using the four-dimensional variational data assimilation technique was developed and applied to a line-shaped, local heavy rainfall event that formed on 19 August 2009 over Okinawa Island, Japan.

First, to identify the primary factors affecting rainband initiation, we performed impact tests using the Japan Meteorological Agency non-hydrostatic model (JMANHM) with 5-km horizontal grid spacing. Simulations in which the orography of Okinawa was removed successfully reproduced the rainband over southern Okinawa, which showed that the primary factor leading to rainband initiation was land surface heating. However, the timing of rainband initiation in these experiments was delayed, and the rainfall intensities were weaker than those observed.

To reduce these discrepancies, we first conducted a high-resolution numerical experiment using JMANHM with 2-km horizontal grid spacing (NODA) followed by data assimilation experiments with GPS observations (i.e., GPS zenith total delay (GPS-ZTD), GPS precipitable water vapor (GPS-PWV), and GPS slant total delay (GPS-STD)) at the same resolution. As a result, increasing the horizontal resolution improved the simulation of the rainfall intensity. Generally, compared with NODA, the assimilations of GPS-ZTD and GPS-PWV are known to slightly improve the timing of the subsequent rainband initiation. However, the GPS-STD assimilation significantly improved the water vapor and temperature fields over a wide area and yielded a clearly improved forecast in terms of both rainfall timing and intensity.

Keywords assimilation; mesoscale convective system; nonhydrostatic; 4d-var; gps; slant total delay

1. Introduction

The growth of cities has increased vulnerability to natural disasters. For example, flooding of small rivers within some Japanese cities as a result of rapidly developing thunderstorms has become a societal problem. One such urban disaster occurred on Okinawa Island, Japan, on 19 August 2009, when flash flooding induced by a small convective system claimed the lives of four workers assessing the seismic capacity of a bridge. This thunderstorm was difficult to

predict because of its small horizontal scale (2–4 km), although the rainband in which the thunderstorm was embedded was predicted by advanced numerical prediction systems. Stationary mesoscale convective systems (MCSs) consisting of several cumulonimbus cloud systems are frequently observed over Okinawa in summer. These MCSs often form a line-shaped rainband and are observed to develop even in the absence of strong synoptic forcing by a typhoon or a Baiu front.

Such rainbands are likely affected by the orography of the island. For example, Chang and Yoshizaki (1991) simulated an MCS observed over Okinawa with a two-dimensional numerical model and concluded that the initiation and movement of the MCS were forced by interactions between the mountains on the island and a cold pool created by the MCS. Minda et al.

───────────────
Corresponding author: Takuya Kawabata, Forecast Research Division, Meteorological Research Institute, Japan Meteorological Agency, 1-1 Nagamine, Tsukuba, Ibaraki 305-0052, Japan
E-mail: tkawabat@mri-jma.go.jp

(2010) also investigated the initiation process of MCSs over Okinawa by using Doppler radar observations and numerical simulations with a 250-m grid spacing. They conducted impact tests with and without incorporating mountain effects and reported that similar MCSs were reproduced in both simulations; however, the sea-breeze circulation was somewhat stronger when the mountain effects were included. Mikami et al. (2011) investigated the evolution of a small convective system over Okinawa by conducting a 1-km numerical simulation with wind profiler and radio acoustic sounding system (RASS) observations. They reported that the convective system developed when the sea-breeze circulation reduced the vertical atmospheric stability.

Although these various numerical simulations reproduced their target phenomena (MCS or convective system), Chang and Yoshizaki (1991) used a two-dimensional model, whereas Minda et al. (2010) and Mikami et al. (2011) used high-performance numerical models but downscaled (so-called "cold start") initial conditions in their studies. From the viewpoint of weather forecasting, predicting the timing and location of an MCS or convective system is particularly important. However, these previous studies did not address timing and location; rather, they were primarily concerned with MCS characteristics or structures. To improve timing and location forecasts, high-performance models that incorporate detailed physical processes (i.e., cloud microphysics and surface processes) and have high horizontal resolution should be used, and observational data should be assimilated to modify the initial water vapor and thermodynamics fields. Therefore, in this study, we used a three-dimensional high-performance model with high horizontal resolution that included cloud microphysics and used an advanced four-dimensional variational (4D-Var) data assimilation system.

To investigate how forecasts of the timing and location of an MCS might be improved, we performed three sets of numerical experiments. First, we examined the effect of the topography of Okinawa Island on the rainfall distribution and timing predicted by the Japan Meteorological Agency non-hydrostatic model (JMANHM) with 5-km horizontal grid spacing. In general, numerical models with similar grid spacing can reproduce rainfall distributions of MCSs rather well, but they are poor at forecasting rainfall intensity and timing. The rainfall intensity forecast can be improved by increasing the horizontal resolution and by considering cloud microphysics. Therefore, we next carried out experiments using a model with a 2-km

horizontal resolution and cloud microphysics. To further improve rainfall forecasts, the initial conditions should be improved by using an advanced data assimilation system to assimilate observations with high horizontal and temporal resolution. Therefore, we developed a data assimilation method for slant total delay (STD) data derived from global positioning system (GPS) observations and used an advanced cloud-resolving nonhydrostatic four-dimensional variational system (NHM-4DVAR; Kawabata et al. 2011) in order to conduct GPS-STD data assimilation experiments.

GPS-STD is the atmospheric delay of radio waves traveling from a GPS satellite to a ground-based receiver; GPS zenith total delay (GPS-ZTD) is the atmospheric delay directly above the receiver; and GPS precipitable water vapor (GPS-PWV) is the cumulative value of precipitable water vapor observations directly above a receiver. The advantage of GPS-STD is that it includes information about several atmospheric parameters (pressure, temperature, and humidity) in several directions from each receiver. Therefore, the assimilation of GPS-STD data improves the water-vapor field with thermodynamics field of the model above and around observation points. The Geospatial Information Authority of Japan has deployed about 1200 GPS receivers throughout Japan that are operated year-round. JMA began to use high-density GPS-PWV observations in its operational mesoscale data assimilation system in 2009. In this study, we used GPS-STD observations obtained by the same observation network.

Ha et al. (2003) carried out an observation system simulation experiment (OSSE) using GPS slant water vapor observations, which are accumulated along slant paths from GPS satellites to receivers (GPS-SW), derived from a virtual GPS observation network. The advantage of GPS-SW data compared with GPS-PWV observations is that information is obtained in various directions from each receiver. Using a fifth-generation mesoscale model (MM5)-4D-Var system (Zou and Kuo 1996) with 27-km horizontal grid spacing to assimilate GPS-SW observations, Ha et al. (2003) obtained good squall-line simulation results. Järvinen et al. (2007) used a high resolution local-area-modeling three-dimensional variational system (HIRLAM; Gustafsson et al. 2001) with 9-km horizontal grid spacing for GPS-STD assimilation, and demonstrated that the magnitude of the GPS-STD assimilation analysis increments exceeded that of the GPS-ZTD assimilation analysis increments, and that the horizontal distribution of analysis increments differed between

the GPS-STD and GPS-ZTD assimilations. Bauer et al. (2011) examined the impact of GPS-STD assimilation on quantitative precipitation forecasting (QPF) with the MM5-4D-Var system and found that the GPS-STD assimilation improved QPF scores. They used two types of initial fields for 24-h forecasts, a downscaled initial field based on operational forecasts of the European Centre for Medium-Range Weather Forecasts and a modified initial field derived from GPS-STD assimilation. Although they were able to demonstrate the advantages of GPS-STD assimilation on the basis of the QPF scores over a one-month period, the horizontal grid spacing of their assimilation system was 18 km. To the best of our knowledge, 4D-Var assimilation of GPS-STD data at storm scale has yet to be performed.

GPS-STD observations include both vertical and horizontal information about the atmosphere, whereas GPS-ZTD and GPS-PWV observations include only vertical information. Thus, in assimilations of GPS-STD observations it is important to take advantage of the horizontal information. For instance, the point at which a slanted path with a 30° elevation angle crosses the troposphere is 17 km (horizontal distance) from the GPS receiver. Thus, if the assimilation system has 20-km horizontal grid spacing, the GPS-STD data cover only two model grid cells. As a result, the expected assimilation effect would be similar to the GPS-ZTD assimilation effect. The NHM-4D-VAR system used in this study has 2-km horizontal grid spacing. Thus, we expected that our numerical simulations would demonstrate more distinct impacts of GPS-STD assimilation than was possible with the lower resolution systems.

In this paper, we introduce the target rainband in Section 2 and describe the NHM-4D-VAR and the GPS-STD assimilation methods in Section 3. In Section 4, we present downscaled forecasts and results, and we discuss the assimilation results in Section 5. Section 6 is a summary with concluding remarks.

2. Local heavy rainfall on 19 August 2009 in Okinawa

Okinawa is a subtropical island located between the four main Japanese islands and Taiwan (Fig. 1). It is 3–30 km wide and 110 km long, extending from southwest to northeast. The northern half of the island is characterized by mountains with elevations greater than 200 m above sea level, whereas the southern half is relatively flat and stands at elevations of less than several tens of meters.

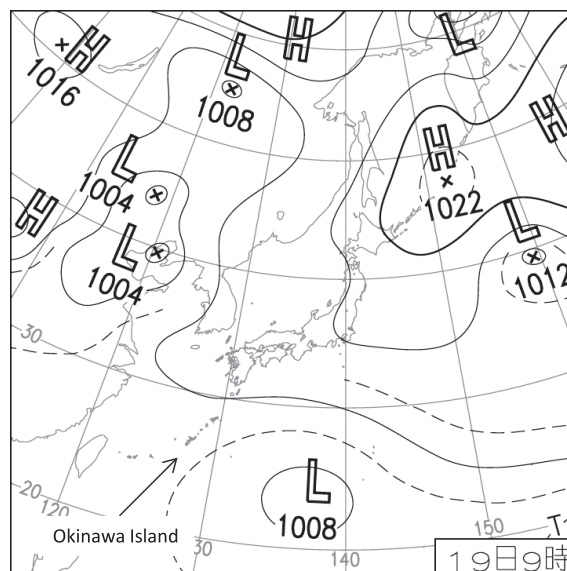The surface weather map for 0900 JST (Japan

Fig. 1. Surface weather map at 0900 JST on 19 August 2009.

Standard Time: UTC + 9 h) on 19 August 2009 (Fig. 1) shows a high-pressure system over the Japanese islands and a weak low-pressure area south of the islands. No strong synoptic forcing, such as a typhoon or a Baiu front, is visible around Okinawa. The surface wind on this date was dominantly northeasterly; thus, the prevailing wind was blowing parallel to the long axis of Okinawa Island. The wind speeds measured on Okinawa at 0600 JST on 19 August were 3–5 m s^{-1}, and the surface temperatures were 26–27°C. By 1200 JST, the wind speeds and the surface temperatures had increased to 4–7 m s^{-1} and to 29–33°C, respectively.

Sporadic convective clouds over Okinawa began to form a line-shaped MCS, aligned along the island's long axis, at around 1130 JST on 19 August 2009 (Fig. 2). This MCS intensified until 1400 to 1500 JST and then vanished at around 1530 JST. The horizontal distribution of the 1-h accumulated rainfall amounts observed by the JMA operational radars and calibrated by the JMA surface rain gauge observations (Fig. 2) shows that the MCS was 200 km long and 30 km wide. The maximum rainfall intensity, observed at 1400 JST, was 52 mm h^{-1}.

The accident referred to in the introduction (Section 1) occurred on the Ga-bu River, 5 km east-northeast from Naha Airport (indicated by the cross in Fig. 3). The total rainfall amount recorded at Naha airport between 1210 and 1400 JST (Fig. 4) was 58.5 mm, and
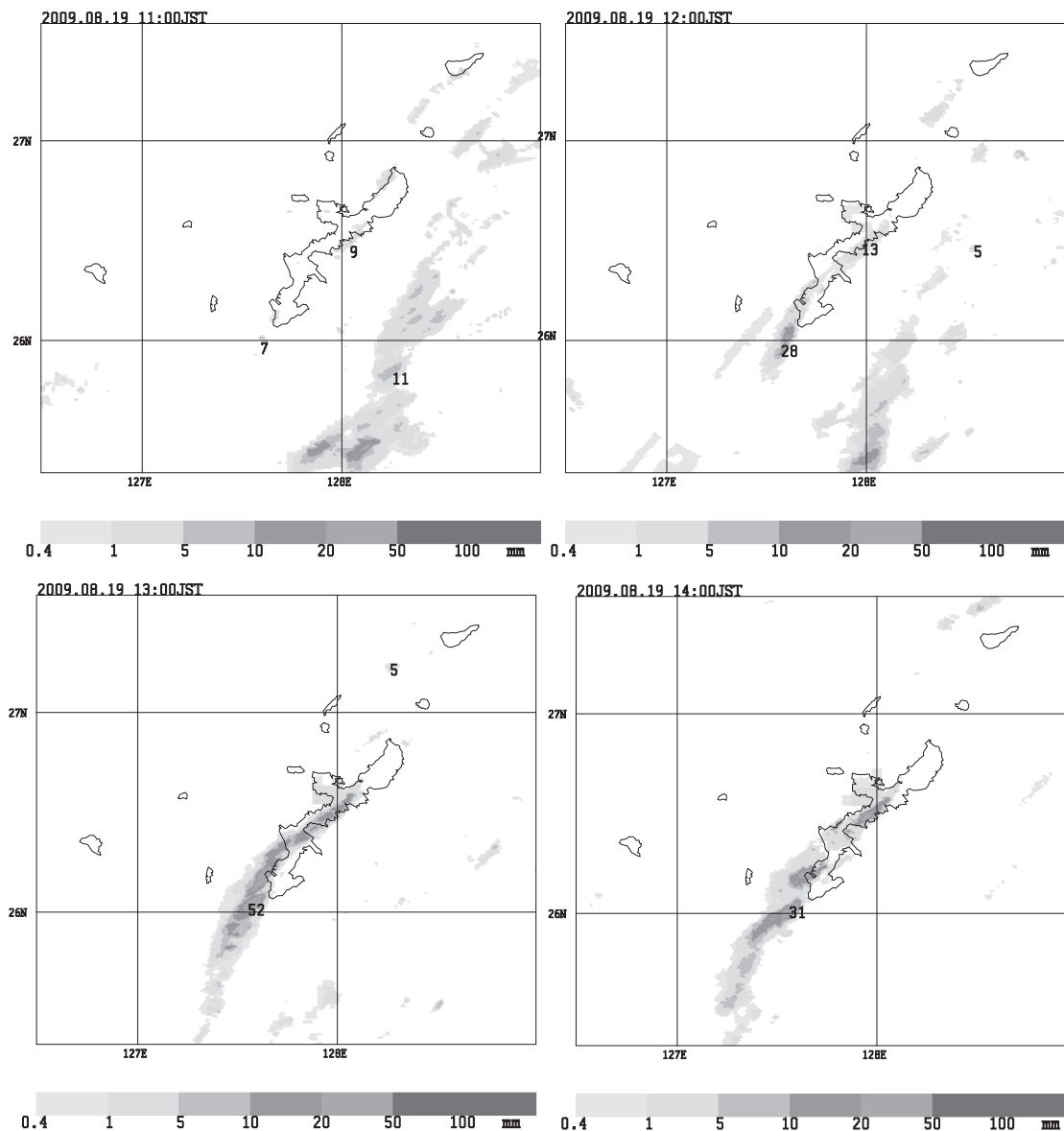
Fig. 2.   Horizontal distributions of 1-h accumulated rainfall amounts from 1100 to 1400 JST on 19 August 2009.

the maximum rainfall intensity was 13.5 mm 10 min^{-1}. The locally heavy rainfall around the Ga-bu River (Fig. 3) that led to the loss of human life was caused by this convective system. Near the headwaters of the Ga-bu River, the rainfall intensity reached 32 mm h^{-1} and caused freshet in the Ga-bu River, which flows between concrete walls, and the flood carried away four workers who were investigating the seismic capacity of a bridge. Similar disasters can occur along the many rivers located near cities in Japan. However,

the smallness of the temporal and spatial scales of such mesoscale events inhibited predicting the development of similar convective systems by current numerical weather prediction systems.

3.   Assimilation method

3.1   NHM-4DVAR

NHM-4DVAR is based on the JMANHM and is designed to reproduce and predict MCSs at cloud-resolving scale. We adopted the full model of
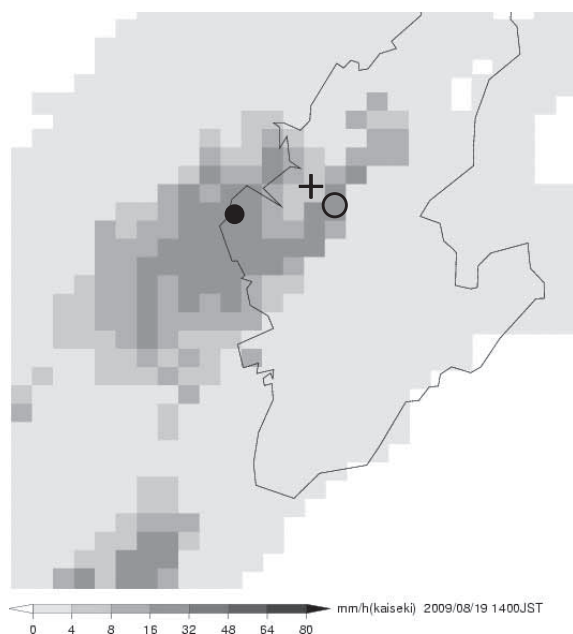
Fig. 3. Horizontal distribution of 1-h accumulated rainfall amounts around the Ga-bu River at 1400 JST. Size of each box is 1 km × 1 km. The cross mark indicates the accident point (on the Ga-bu River), and the open circle indicates the headwaters of the Ga-bu River. The solid black circle indicates Naha airport. The coastline of Okinawa Island is also shown.
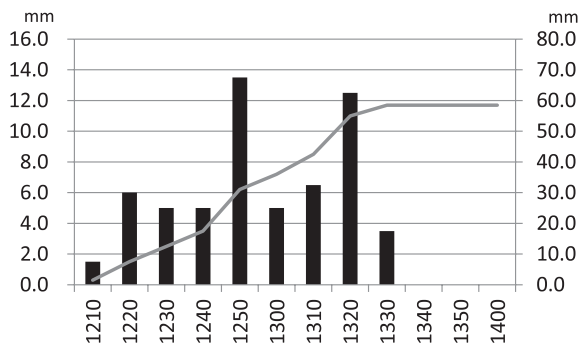

Fig. 4. Time series of 10-min rainfall amounts (bars; left axis) and accumulated amount (line; right axis) at Naha airport, shown as a solid black circle in Fig. 3.

JMANHM (Saito et al. 2006), which includes three-ice bulk cloud microphysics, as the forward model. In the first version of NHM-4DVAR (Kawabata et al. 2007), the adjoint model considered only dry dynamics and advection of water vapor. Kawabata et al. (2011) implemented an additional warm rain process for assimilating radar reflectivity. The horizontal resolution of NHM-4DVAR is 2 km. The control variables are the three wind components, potential temperature, surface pressure, nonhydrostatic pressure, total water (water vapor and cloud water), the relative mixing ratio of rainwater, and the pseudo-relative humidity (only for lateral boundary conditions).

3.2   Assimilation of GPS slant total delay data
a.   Observation operator

GPS-STD is affected by the atmosphere along the ray path. Shoji et al. (2004) decomposed GPS-STD data into three components, isotropy, first-order horizontal gradient, and higher order inhomogeneity and showed that the horizontal scale of each component was different—approximately 600, 60, and

2–3 km, respectively. GPS-ZTD data represent only the isotropic component of GPS-STD data observed simultaneously at the same site, and GPS-PWV data consist of only the isotropic water vapor information contained within the GPS-ZTD data. This study represents an attempt to fully utilize the GPS-STD data. In this section, we describe an observation operator for GPS-STD data.

Radio waves from GPS satellites in orbits higher than 20,000 km are delayed by various factors, and GPS meteorology applications that take advantage of this atmospheric delay have been developed (e.g., Shoji 2009). The speed of radio waves is less in atmosphere than in a vacuum. This atmospheric delay effect can be described in terms of the refractive index n as follows:

$$n = \frac{c_0}{c} > 1, \tag{1}$$

where c_0 and c represent the speed of light in a vacuum and the atmosphere, respectively. The general equation for the radio refractive index is

$$n = 1 + \left(K_1 \left(\frac{P_d}{T} \right) + K_2 \left(\frac{P_v}{T} \right) + K_3 \left(\frac{P_v}{T^2} \right) \right) \times 10^{-6}, \tag{2}$$

where P_d (hPa) and P_v (hPa) denote the partial dry atmospheric pressure and the partial water vapor pressure, and T (K) denotes the temperature. K_1 is 77.60 K hPa^{-1}, K_2 is 71.98 K hPa^{-1}, and K_3 is 3.754 × 10^5 K^2 hPa^{-1} (Boudouris 1963). Equations 1 and 2 both show that a radio wave traveling in the atmosphere takes a longer time to go a given distance than one traveling in a vacuum. The delay can be measured in terms of distance L as follows:

$$\Delta L = \int_{Model\_surface}^{Model\_top} (n-1)\,ds. \qquad (3)$$

Here, ΔL denotes the atmospheric delay (m), ds is the path length (m) in each model grid cell, and n denotes the average refractive index along the path in a grid cell.

In this study, we considered the effect of the earth's curvature but assumed that the radio waves propagated along straight pathways; thus, the bending effect is ignored. This assumption may lead to errors at low GPS satellite elevation angles. As described in Section 3.2b, we applied large observational errors to low elevation angles so that the linear assumption would not lead to serious problems. First, the linear path from the receiver to the GPS satellite is determined. Then the coordinates of the middle point of the path within the model grid cells are calculated. Delays at eight points surrounding the middle point are interpolated to the middle point and averaged with each distance. The delay at the point is multiplied by the length of the path within the model cell, and then the delays in cells along the path are integrated from the surface to the top of the model. We used GPS-STD observations with path elevation angles of 5° or more in this study. The World Geodetic System 1984 (WGS84; National Imagery and Mapping Agency 1997) is adopted as the reference GPS coordinate system. Therefore, WGS84 is used in the observation operator.

It is necessary to add the atmospheric delay above the model top (22 km in this study) to the left side of Eq. (3). We assumed that the delay decreased to 1/e every 10 km from the model top to a height of 200 km (Bean and Thayer 1959) and that above 200 km the amount of delay was zero.

We also ignored perturbations in the dry atmospheric pressure (P_d) in the adjoint code of the observation operator (Eq. 2) because such perturbations sometimes produce noise in pressure in NHM-4DVAR, which contains no penalty term to alleviate such noise. We also ignored perturbations in the air density in the GPS-PWV assimilation for the same reason (Kawabata et al. 2007). In preliminary sensitivity experiments, we confirmed that inclusion of pressure perturbations had negligible impact on the rainfall forecast (not shown).

b. Observational error

Because the average distance between GPS receivers in Japan is about 20 km, high cross-correlations may exist in observational errors between receivers if the slant paths are close together. We examined correlations among GPS-STD values as
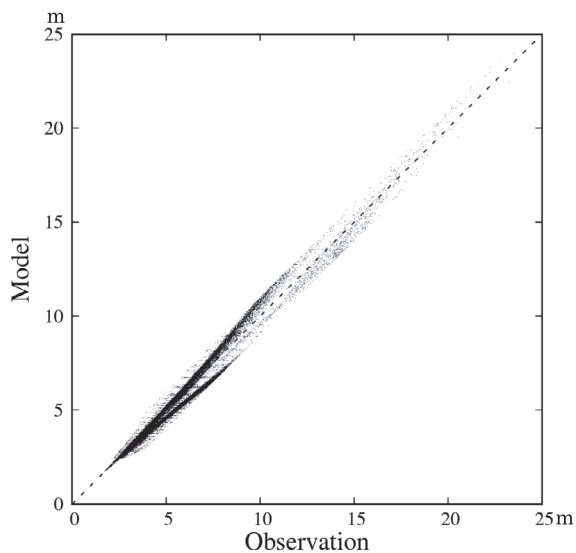

Fig. 5. GPS slant total delay values (m) in simulations (vertical axis) and observations (horizontal axis).

follows. First, we constructed data sets of GPS-STD values derived from two GPS satellites observed by a single GPS receiver and calculated the correlation between the two sets of observations. Observations were made every 5 min from 0900 to 1500 JST on 19 August 2009 by the method of Shoji (2013). The resulting correlation coefficient averaged over all observations was −0.02. Even when the angle between the paths from the receiver to each of the two satellites was less than 30°, a situation that accounted for only 6% of all the data, the correlation coefficient was just 0.4. Therefore, correlations between individual GPS-STD observational errors are generally small. Thus, for simplicity, we assumed that the GPS-STD observational error covariance matrix was a diagonal matrix.

"Observational errors" in data assimilation are composed of measurement error and observation operator error. To evaluate the latter error, we constructed another data set of model-predicted STDs. A JMANHM simulation was carried out using a horizontal grid with a spacing of 2 km and the JMA operational mesoscale analysis was used for the initial and boundary conditions. The examination domain was almost the entire area of the Japanese islands (not shown). We then plotted the predicted GPS-STDs against the observed slant delay values (Fig. 5) without applying any quality controls to the data. Although the data do not exhibit any apparent bias, the difference

between the predicted and observed delay values is large for values larger than 12 m, and the difference distribution is bimodal at delay values from 5 to 10 m (Fig. 5). This bimodal distribution may be a problem for rigorous assimilation, but we are still investigating its cause, which may be, for example, an insufficient sample size or an inappropriate observation operator.

It is difficult to determine the GPS-STD measurement error because no comparable reliable observations exist. Upper soundings are comparable only in the zenith direction, and because few are available, they cannot be examined statistically. Consequently, we based the value of the observational error mainly on values used by previous studies and on comparisons with GPS-PWV assimilation results.

Bauer et al. (2011) used 1 mm of precipitable water vapor, which is equivalent to 6 mm of GPS-ZTD, as the observational error in the zenith direction. They calculated this error using data from a German observation network and European mesoscale model predictions. Järvinen et al. (2007) inferred a ZTD error of 11 mm from a comparison of modeled and observed STDs.

In this study, we first set the GPS-ZTD observational error to 11 mm, under the assumption that the cost function value of GPS-ZTD should be a few times larger than the GPS-PWV cost function value, because GPS-ZTD data contain more meteorological information than GPS-PWV data.

Because GPS-ZTD uses mapping functions to average several GPS-STDs, GPS-ZTD observations are considered to be more reliable than individual GPS-STDs, even if the elevation angle is high. Furthermore, the observational error depends on the elevation angle. Järvinen et al. (2007) and Bauer et al. (2011) used the same type of error model. By comparing GPS-STD assimilation with GPS-PWV assimilation and considering the GPS-ZTD error, we estimated that the GPS-STD error in the zenith direction was 50 mm and adopted the error model below (Eq. 4).

$$\text{ObsError} = \frac{50 \text{ mm}}{\sin^4 \theta}, \tag{4}$$

where θ denotes the elevation angle. When we used Eq. (4) to compute the observational error, GPS-STD observations at low elevation angles had only a small impact on the assimilation result. The error of 50 mm and that calculated with Eq. (4) are large compared with the values suggested by Järvinen et al. (2007) and Bauer et al. (2011), but we chose to use a conservative value and function for this first GPS-STD assimilation

trial because our assumption of linear propagation (see Section 3.2a) might result in large observational errors at low elevation angles. In addition, when the elevation angle exceeds 85°, the standard deviation of the departure value (observation minus model; Fig. 5) is 35 mm, which is comparable to the 50 mm used in Eq. (4).

On the basis of these considerations and the results of our investigations, we adopted the following quality controls. When the elevation difference between an observation site and the modeled topography exceeded 50 m, the observations were not used (we used this same criterion in our previous GPS assimilation studies; Kawabata et al. 2007, 2011). We also discarded data when the observed delay exceeded 10 m and the absolute value of the departure value exceeded 1 m.

c. Data thinning

The cost function of GPS-STD is still large, despite the use of a large observational error model, because the number of GPS-STD data is very large; therefore, we thinned the GPS-STD data. When two slant total delays from a GPS satellite were observed by two adjacent receivers, one STD value was eliminated and the other was selected. Similarly, if two or more slant delays were observed at the same time, the number of STD observations was thinned by approximately half. The thinning procedure halved the value of the cost function.

4. Numerical experiments with downscaled initial conditions

4.1 Experimental design

Initiation of a rainband on small islands is expected to be caused mainly by (i) uplift in mountainous regions, and (ii) land–sea wind circulation due to contrasting sea and land surface temperatures. In addition, frictional convergence caused by the difference between land- and sea-wind speeds may affect rainband initiation. To investigate the factors responsible for the rainband initiation over Okinawa, we performed three numerical simulations: (a) "CTL." a control experiment using the actual orography and land-surface conditions; (b) "Sea." a simulation in which all islands were treated as sea; and (c) "NoMt." a simulation in which all mountains were flattened and the roughness of the land surface was set to the same value as that of the sea. Thus, in NoMt, updrafts due to uplift along mountain slopes and frictional convergence were eliminated as a cause. The difference in the simulation result between CTL and NoMt mainly represents the mountainous orography effect and the
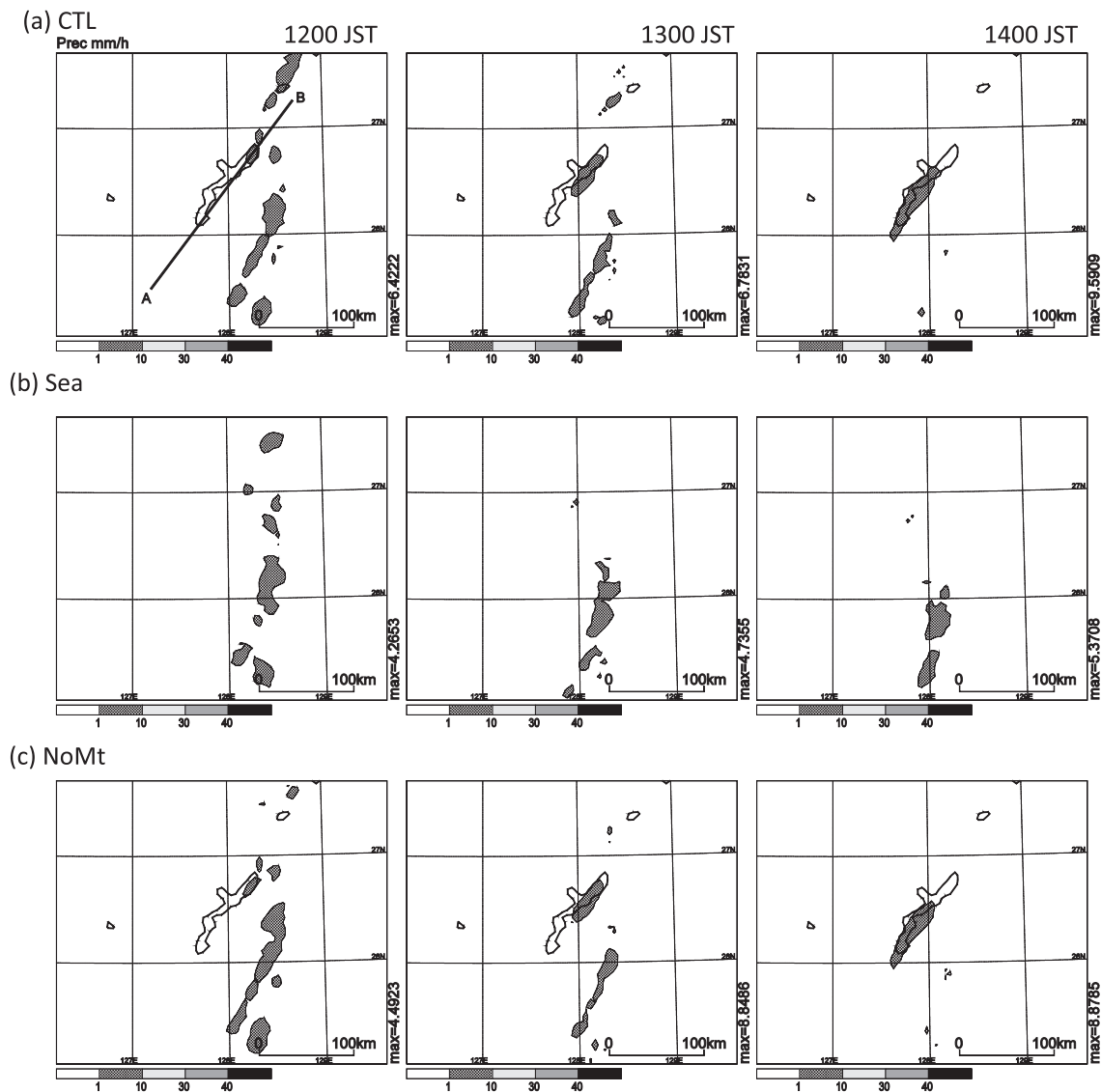
Fig. 6.   1-h rainfall intensity (mm h^{-1}) of CTL (a), Sea (b), and NoMt (c) from 1200 to 1400 JST on 19 August.

difference between NoMt and Sea represents the surface heating effect. In all three simulations, initial conditions were provided by the JMA mesoscale analysis at 2100 JST on 18 August 2009, and boundary conditions were given by the JMA global model forecasts until 1500 JST on 19 August. The horizontal resolution was 5 km. The JMANHM settings, including the Kain–Fritsch convective parameterization, were the same as those of the JMA operational mesoscale model.

4.2   Results of the downscaled experiments

In CTL (Fig. 6a), convective systems developed over northern Okinawa Island at 1200 JST. By 1400 JST, they had organized into a rainband, similar to the observed one. In Sea (Fig. 6b), several convective systems persisted over the ocean for more than 3 h, but they did not organize into a rainband. The convective area in the northern part of the experimental domain had vanished by 1300 JST. In NoMt (Fig. 6c), the distribution and intensity of precipitation were similar to those in CTL. Surface temperatures over southern Okinawa in both CTL and NoMt reached 306 K, close

Fig. 8.   Horizontal distribution of the lifted condensation level (LCL) at z = 128 m at 1200 JST in CTL.
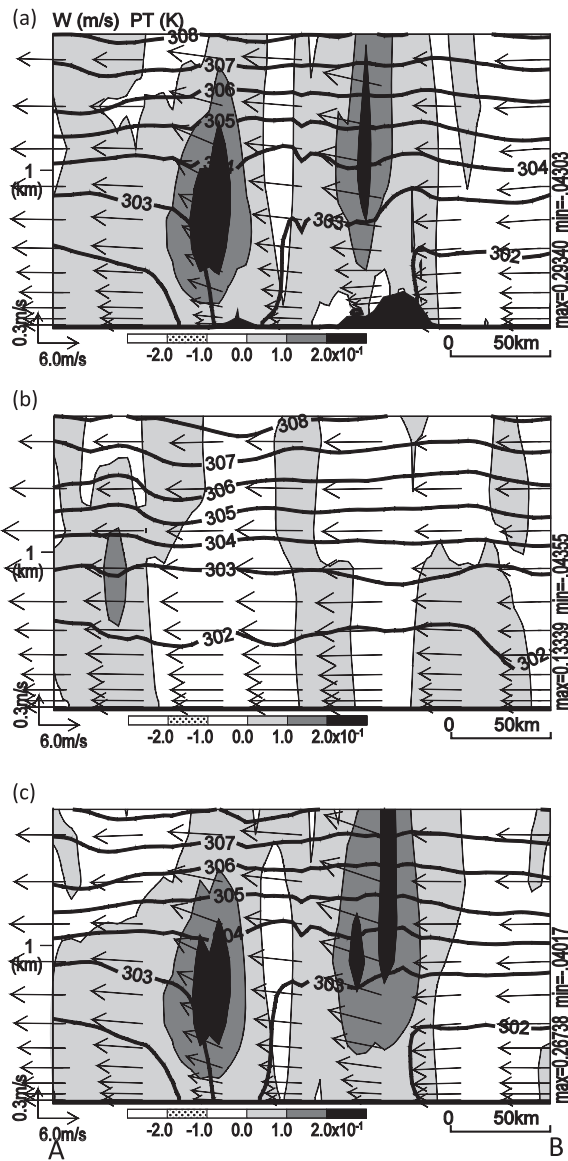
Fig. 7.   Vertical cross sections along line A–B in Fig. 6a of potential temperature (contours), vertical wind speed (shades), and wind projected on the cross section (vectors). CTL (a), Sea (b), and NoMt (c) at 1200 JST.

to the observed value, whereas the surface temperature in Sea was fixed at 301 K, the sea surface temperature. From these results, it is reasonable to infer that surface heating was essential for the rainband production, whereas orographic effects and wind convergence due to surface roughness were not critical in initiating the rainband.

Examination of the results in vertical cross section

along Okinawa's long axis showed that the boundary layer evolved to a height of 1 km over Okinawa in both CTL and NoMt (Figs. 7a, c), whereas in Sea (Fig. 7b), temperature was horizontally homogeneous, and no boundary layer was apparent. The similarity between CTL and NoMt indicates that the mountains in northern Okinawa did not play an important role in the evolution of the boundary layer over the island.

Two major updrafts of speed greater than 0.2 m s^{-1} were simulated in CTL and NoMt, one to windward and the other to leeward over the island, where the top of the boundary layer was higher than it was over the sea. In addition, the wind in the lowest atmospheric layer over the central part of the island was clearly weaker in the CTL and NoMt results than in the Sea result. In NoMt, the roughness of the island land surface was the same as the sea surface roughness, so this weakening was not induced by surface friction. The wind distributions instead suggest the occurrence of land–sea circulation in the boundary layer in CTL and NoMt. Therefore, we inferred that the updrafts simulated in these experiments led to the development of the convective system over the island.

In both CTL and NoMt (Figs. 6a and 6c), only the updraft over northern Okinawa induced a convective system, because vertical stability was greater over southern than over northern Okinawa (Fig. 8). In the north, the height of the lifted condensation level (LCL) was 500 to 600 m, whereas in the south it exceeded 900 m. The relatively stable atmospheric condition in the south depressed the development of convection.
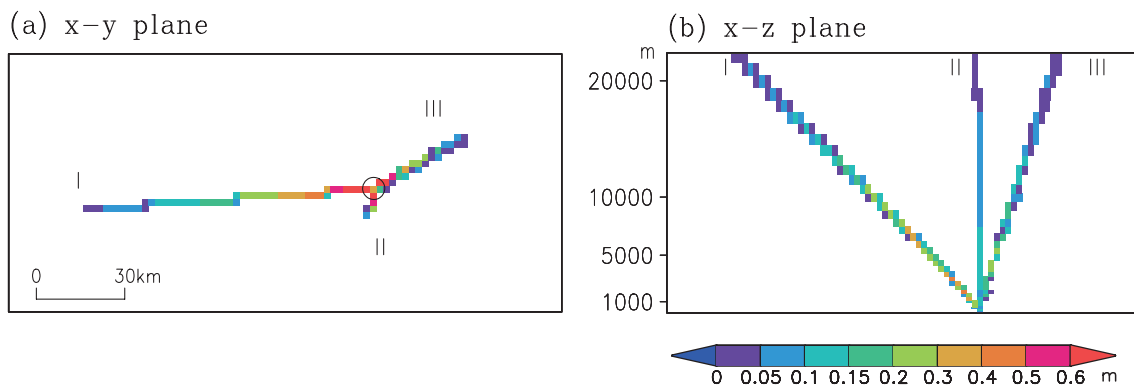
At 1400 JST, the rainbands in CTL (Fig. 6a) and

Fig. 9.   Propagation paths of radio waves from GPS satellites (I, II, and III) to a receiver in the model atmosphere, viewed in the horizontal plane (a) and the vertical plane (b). Colors indicate the delay value in each grid cell (each model grid cell is represented by one pixel). The open circle in (a) shows the position of the GPS receiver (the observation site).

NoMt (Fig. 6c) appeared to be similar to the observed rainband (Fig. 2). These results indicate that the land–sea circulation caused by surface heating of the land initiated rainband development at the same location that the observed rainband was initiated. However, the timing of rainband initiation in CTL and NoMt was delayed compared with the observation. Moreover, the maximum observed rainfall intensity at 1300 JST was 52 mm h^{-1} and that at 1400 JST was 31 mm h^{-1}, whereas in CTL, they were 7 and 10 mm h^{-1}, respectively. In general, a high-resolution simulation with cloud microphysics can enhance the rainfall intensity forecast. However, the comparison of the vertical cross sections in the results for CTL, NoMt, and Sea suggests that atmospheric instability greatly affected the initiation of the rainband. For further improvement of the rainfall forecast, data assimilation that modifies atmospheric instability conditions is necessary. Therefore, we conducted data assimilation experiments with a storm-scale assimilation system for assimilating GPS observations.

5. Data assimilation experiments

5.1 Impact on single analyses at a single site

First, we performed three experiments using NHM-4D-VAR with 2-km horizontal grid spacing in which three GPS-STD observations (SO_STD), one GPS-ZTD observation (SO_ZTD), or one GPS-PWV observation (SO_PWV) from a single observation site were assimilated. As mentioned in Section 3.2a, the GPS-ZTD and GPS-PWV observations were derived from the GPS-STD observations. The purpose of these experiments was to verify the effects of GPS-STD

assimilation on a single analysis result and to examine the differences among GPS-STD, GPS-ZTD, and GPS-PWV assimilations. The length of the assimilation window was 10 min, and the observations were assimilated at 5-min intervals (at 0, 5, and 10 min) in the assimilation window. The observation data were selected by considering their horizontal distributions, elevation angles, and the first-guess field from an experimental data set.

Figure 9 illustrates the propagation paths of radio waves from the three GPS satellites to a receiver in the model atmosphere in both the horizontal (Fig. 9a) and the vertical plane (projected from the south; Fig. 9b). Path I has the smallest angle of elevation among the three paths and is also the longest path, whereas path II, which has an angle of elevation near 90°, is very short. Large delays occur mostly at low altitudes.

The distributions of the analysis increments (analysis minus first guess) of precipitable water vapor in SO_STD (Fig. 10a) and SO_ZTD (Fig. 10b) at the end of the assimilation window differ. In SO_ZTD, the increment distribution (Fig. 10b) is elliptical and almost axisymmetric (i.e., isotropic). Although 4D-Var is capable of producing flow-dependent (anisotropic) analysis increments, the 10-min assimilation window is too short to capture the model dynamics. As a result, the analysis increment distribution in SO_ZTD is almost isotropic. In contrast, the inhomogeneous shape of the analysis increment distribution in SO_STD (Fig. 10a) reflects the distribution of the slant paths. In addition, the maximum analysis increment value is much larger in SO_STD (10 mm; Fig. 10a) than in SO_ZTD (6 mm;
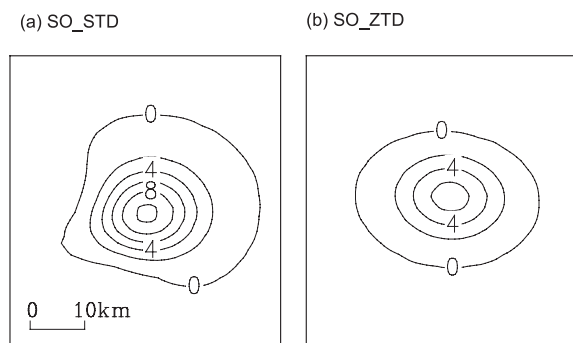
Fig. 10. Analysis increments of precipitable water vapor (mm) at the end of the assimilation window for SO_STD (a) and SO_ZTD (b).

Fig. 10b). The increment distribution in SO_PWV was similar to that in SO_ZTD (not shown).

In vertical cross sections of the analysis increments of the mixing ratio of water vapor (Qv) and potential temperature (PT) along path III (Fig. 11), the increment distributions of SO_ZTD and SO_PWV are similar, and the increment magnitudes are nearly the same: the distributions of both Qv and PT increments extend vertically from 1 to 5 km height and horizontally a distance of 5−8 km. In contrast, in SO_STD the increment distribution along path III extends horizontally a distance of 15 km and vertically to a height exceeding 8 km; moreover, the increment magnitudes are much greater, especially at low altitude (around 3 km). The magnitude of the assimilation increments is large because all of the slant paths are within a narrow area of the lower troposphere above the observation site. Total weights in the cost function were similar among the SO_STD, SO_ZTD, and SO_PWV assimilations, but their effects are seen at different places.

5.2 Design of actual 30-min assimilation experiments

We next conducted high-resolution data assimilation and forecast experiments using NHM-4DVAR with 2-km horizontal grid spacing and an assimilation window of 30 min. In these experiments, multiple actual observations were assimilated, and extended 3-h forecasts were produced by the 4D-Var analysis. The forecast result described in Section 4 (CTL) was used as the first-guess field and for the lateral boundary conditions. The 30-min assimilation was started at 1100 JST on 19 August, and the forecast was

performed from 1100 to 1400 JST using the assimilation result as the initial conditions (Fig. 12). We conducted three experiments in which GPS-STD, GPS-ZTD, or GPS-PWV data were assimilated every 10 min (hereafter, STD, ZTD, and PWV, respectively). Only the observations listed above were assimilated. A fourth experiment, in which no data were assimilated, was called NODA. No cumulus parameterization was used in the data assimilation and 3-h forecasts. Figure 13 shows the assimilation and forecast domains and the distribution of GPS observation sites used for the experiment. The distributions of GPS-STDs in the model atmosphere at each assimilation time (1100, 1110, 1120, and 1130 JST; Fig. 14) show that unlike the GPS-PWV and GPS-ZTD data sets, the GPS-STD data contain a great deal of horizontal information.

5.3 Results of the multi-observation assimilations with a 30-min window and forecasts

The time evolution and horizontal distribution of rainfall in NODA from 1200 to 1400 JST (Fig. 15a) were similar to those in CTL (Fig. 6a), but the maximum rainfall intensity was enhanced to 21 mm h^{-1} at 1300 JST. This improvement in NODA resulted from the increase in the horizontal resolution and the removal of the cumulus parameterization. The horizontal rainfall distributions in ZTD and PWV (Figs. 15b and 15c) resembled the rainfall distributions in NODA; however, in both ZTD and PWV, a rainband formed near southern Okinawa at 1300 JST, while simultaneously, the rainfall intensity over northern Okinawa was strengthened to 24 mm h^{-1}. These results demonstrate that increasing the horizontal resolution improves the rainfall intensity forecast and that the assimilation of GPS-ZTD and GPS-PWV data slightly improves the timing of the subsequent rainband initiation.

In STD (Fig. 15d), regions of intense rainfall had already formed over southern and southwestern Okinawa at 1200 JST, and the maximum intensity reached 47 mm h^{-1}. By 1300 JST, a rainband had formed over the island, but rainfall intensity had weakened slightly to 25 mm h^{-1}. Thus, the assimilation of GPS-STD data improved the rainfall forecast with respect to both timing and intensity compared with the assimilation of GPS-PWV and GPS-ZTD data.

Comparison of PT differences between NODA and STD revealed an area of large positive increments at heights of 500–1500 m over the southern end of Okinawa Island and one of large negative increments at heights of 1000–2000 m over central Okinawa (Fig.
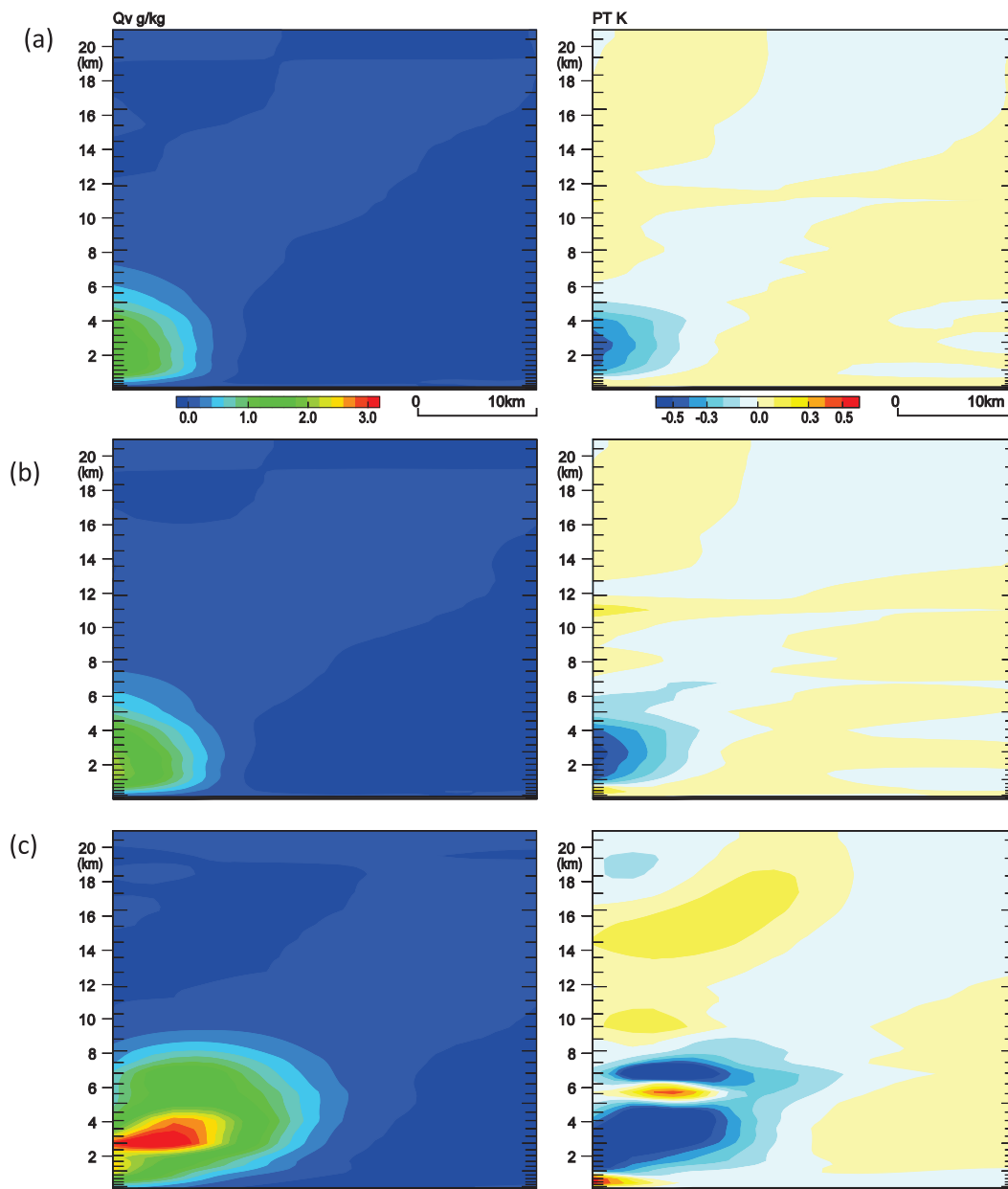
Fig. 11.   Vertical cross sections along path III. Analysis increments of the mixing ratio of water vapor is shown in the left column and potential temperature in the right column. SO_PWV (a), SO_ZTD (b), and SO_STD (c). The observation site is at the lower left corner of each panel, and path III leaves the model top at the upper right corner.

16a). Both Qv (Fig. 16b) and vertical wind speed (Fig. 16c) were increased where the mixing ratio of the cloud water was enhanced in STD. These modifications due to the assimilation of GPS-STD data led to the production of cloud water and an increase in PT on account of condensation heating. Furthermore, there is

an area of weak positive PT increments below the area of negative increments. This positive increment area is within the boundary layer, where it contributed to a decrease in vertical stability. In this positive PT region, the updraft was strengthened and Qv was increased in STD as well. These modifications enhanced vertical
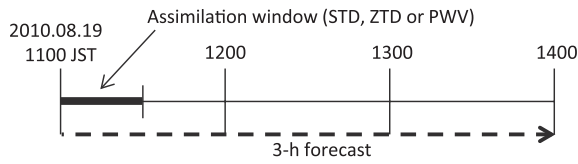
Fig. 12. Schematic diagram of the data assimilation and forecast experiment.

Fig. 13. The assimilation and forecast domain, topography and GPS observation stations.
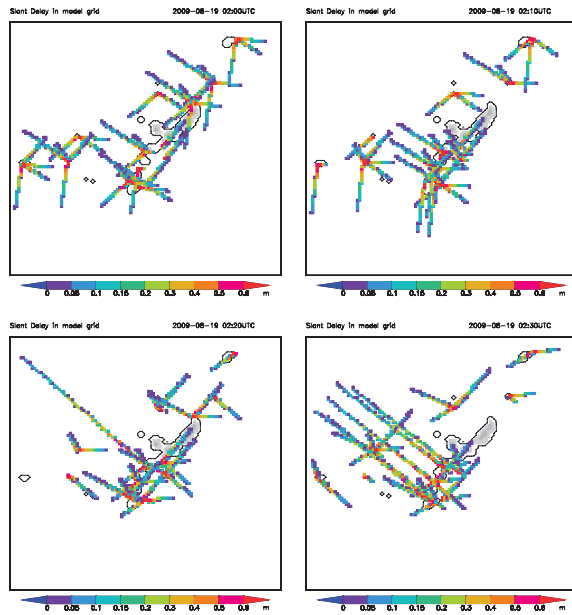

Fig. 14. Propagation paths of radio waves from GPS satellites to receivers in the model atmosphere, viewed in the horizontal plane. Real slant delay observations obtained over Okinawa Island at 1100 JST (upper left), 1110 JST (upper right), 1120 JST (lower left), and 1130 JST (lower right) on 19 August 2009.

instability and contributed to the improved timing of the rainfall forecast.

The LCL results also show increased vertical instability in the GPS-STD assimilation over southern Okinawa. A stable region in NODA (Fig. 17a), indicated by LCLs of 800–900 m above southern Okinawa (similar to CTL, see Fig. 8), became less stable in STD (Fig. 17b). As a result of this increased instability in STD, convective regions began to develop over Okinawa, and the later rainfall forecast was improved compared with that in NODA.

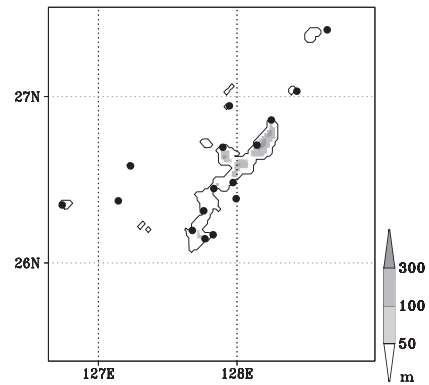From these results, we conclude that increasing the horizontal resolution and the removal of cumulus

parameterization contributed to an improved rainfall intensity forecast (NODA), assimilation of GPS-PWV or GPS-ZTD slightly improved the timing of the rainfall forecast, and modifying the vertical thermodynamic profile by GPS-STD assimilation further improved the forecast with respect to both rainfall intensity and timing.

6. Summary and concluding remarks

MCSs are often induced over Okinawa Island in summer. We therefore investigated the mechanisms responsible for the initiation of a rainband that formed on 19 August 2009. The rainband, which began to form at 1100 JST, had developed into a linear feature by 1200 JST and lasted until around 1600 JST.

We first investigated the factors affecting the initiation of the rainband by performing three experiments using JMANHM with 5-km horizontal grid spacing: a downscaled numerical experiment (i.e., "CTL"), an experiment in which the islands in the model were replaced by sea (i.e., "Sea"), and one in which the islands were treated as flat planes and the surface roughness of the ground was set to the same value as that of the sea (i.e., "NoMt"). In Sea, a linear MCS did not form, whereas a rainband similar to the observed rainband developed in CTL and NoMt. The rainbands in CTL and NoMt were induced by boundary layer evolution and sea–land wind circulation over Okinawa. These results indicate that the primary factor inducing rainband formation over Okinawa is surface heating, and that updrafts caused by mountains and wind convergence caused by surface friction are not primary factors in rainband initiation. Though the rainbands were initiated in CTL and NoMt
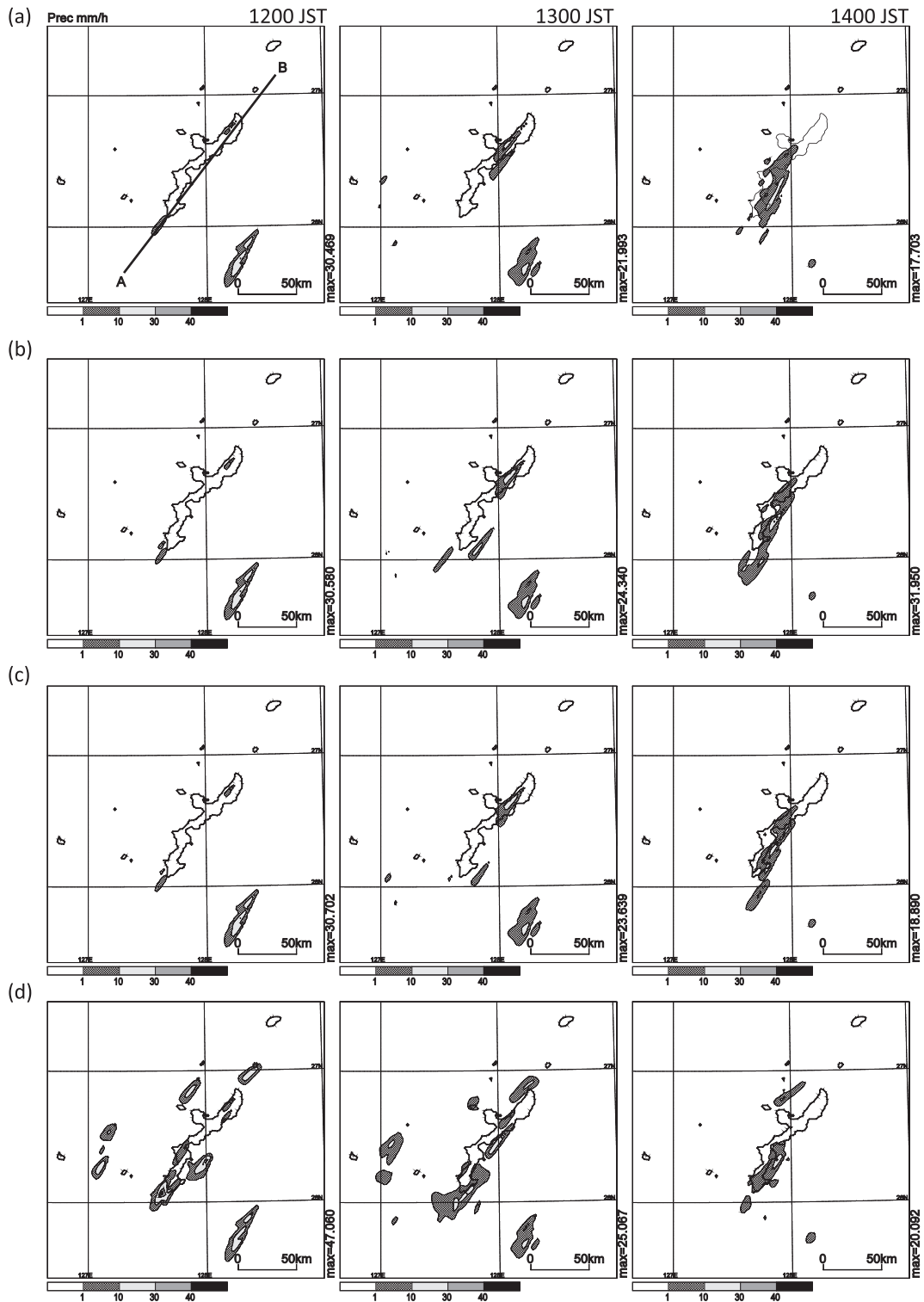
Fig. 15.   Horizontal distribution of 1-h accumulated rainfall amount from 1200 (forecast time (FT) = 01) to 1400 (FT = 03) JST. NODA (a), PWV (b), ZTD (c), and STD (d).
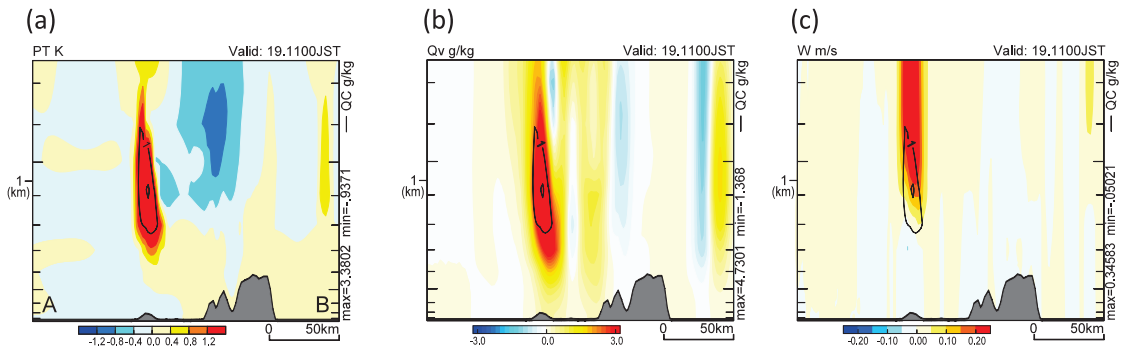
Fig. 16. Vertical cross sections along line A−B in Fig. 15a showing differences of potential temperature (shaded) (a), the mixing ratio of water vapor (shaded) (b), and vertical wind speed (shaded) (c) (STD minus NODA), and the mixing ratio of cloud water in STD (contours) (all panels), at 1100 JST (FT = 00).
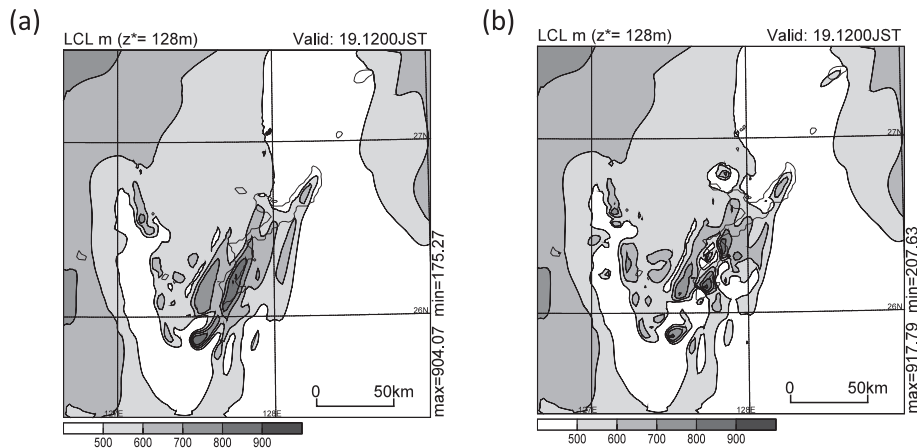

Fig. 17. Same as Fig. 8 but in NODA (a) and STD (b) at 1200 JST.

at the same location as the observed rainband, the predicted rainfall was delayed and its intensity was weaker than the observed. Further, both CTL and NoMt failed to reproduce the observed rainfall over southern Okinawa.

To address these problems, we next conducted high-resolution simulations with data assimilation using NHM-4DVAR with 2-km horizontal grid spacing. When we developed the observation operator for GPS-STD assimilation, we assumed linear propagation of the radio waves. We also adopted an elevation-dependent observation error model and data thinning to keep the magnitude of the GPS-STD cost function reasonable compared with that of the GPS-PWV cost function.

First, we examined differences in the impact of

assimilations of GPS-STD, GPS-ZTD, and GPS-PWV observations from a single observation site on a single analysis result. The GPS-ZTD and GPS-PWV assimilation results were similar in their basic features. The distributions of the analysis increments obtained by the GPS-PWV and GPS-ZTD assimilations were approximately circular, whereas the increment distribution obtained by GPS-STD reflected the inhomogeneous data distribution. Moreover, analysis increments at low altitudes were larger in the GPS-STD assimilation than in the GPS-ZTD or GPS-PWV assimilations. These results demonstrate that more horizontal atmospheric information is included in GPS-STD assimilation, and that the effects of GPS-STD assimilation are large at low atmospheric levels above the observation site.

Next, we conducted data assimilation experiments with 2-km horizontal resolution using multiple actual observations from different sites. The forecast from the first-guess field (NODA) indicated that increasing the horizontal resolution resulted in greater rainfall intensity than in the 5-km downscaled experiment (CTL). The GPS-ZTD and GPS-PWV assimilations produced improved forecasts compared to NODA, but there remained timing and positional lags. The GPS-STD assimilation clearly improved the forecast of both the timing and intensity of the rainfall. This improved forecast reflected the decreased atmospheric stability over Okinawa, especially over southern Okinawa, and the improvement of the initial conditions around the island that resulted from the assimilation of GPS-STD data.

GPS-STD data include information about temperature, dry atmospheric pressure, and water vapor pressure (see Eq. 2). In addition, GPS-STD data contain both horizontal and vertical information about those atmospheric elements. Atmospheric inhomogeneity is greatest in the lower troposphere (1–4 km height; see figure 1b of Shoji 2013). Assimilating GPS-STD data that included information on the distribution of humid air improved the rainband forecasts. A GPS signal following a path with a 15° elevation angle travels about 11 km horizontally and propagates vertically 3 km. Therefore, the high-resolution data assimilation system used in this study was able to take advantage of the additional information in the GPS-STD data. Larger analysis increments were obtained in the lower troposphere by the high-resolution 4D-Var data assimilation system with GPS-STD assimilation than with GPS-ZTD or GPS-PWV assimilation (see Section 5.1). As a result, in subsequent experiments that assimilated actual observation data, GPS-STD assimilation resulted in improved simulation of atmospheric conditions compared with GPS-ZTD or GPS-PWV assimilation.

In future work, the observational error model and the data thinning method used in this study should be updated and made more sophisticated. In addition, the assumption of linear propagation (neglecting the bending effect) needs to be removed, because it introduces errors in low-elevation observations.

Acknowledgments

References

Bauer, H.-S., V. Wulfmeyer, T. Schwitalla, F. Zus, and M. Grzeschik, 2011: Operational assimilation of GPS slant path delay measurements into the MM5 4DVAR system. *Tellus A*, **63**, 263–282.

Bean, B. R., and G. D. Thayer, 1959: Central radio propagation laboratory exponential reference atmosphere. *NBS Journal of Reseach D*, **63**, 315–317.

Boudouris, G., 1963: On the index of refraction of the air, the absorption and dispersion of centimeter waves by gasses. *Journal of Reseach*, **67**, 631–684.

Chang, C., and M. Yoshizaki, 1991: A numerical study of the mesoscale convective system observed over Okinawa Island in Jun 1987. *Mon. Wea. Rev.*, **119**, 2724–2733.

Gustafsson, N., L. Berre, S. Hörnquist, X-Y. Huang, M. Lindskog, B. Navascués, K. S. Mogensen, and S. Thorsteinsson, 2001: Three-dimensional variational data assimilation for a limited area model. Part I: General formulation and the background error constraint. *Tellus A*, **53**, 425–446.

Ha, S., Y.-H. Kuo, Y.-R. Guo, and G.-H. Lim, 2003: Variational assimilation of slant-path wet delay measurements from a hypothetical ground-based GPS network. Part I: Comparison with precipitable water assimilation. *Mon. Wea. Rev.*, **131**, 2635–2655.

Järvinen, H., R. Eresmaa, H. Vedel, K. Salonen, S. Niemelä, and J. de Vries, 2007: A variational data assimilation system for ground-based GPS slant delays. *Quart. J. Roy. Meteor. Soc.*, **133**, 969–980.

Kawabata, T., H. Seko, K. Saito, T. Kuroda, K. Tamiya, T. Tsuyuki, Y. Honda, and Y. Wakazuki, 2007: An assimilation and forecasting experiment of the Nerima heavy rainfall with a cloud-resolving nonhydrostatic 4-dimensional variational data assimilation system. *J. Meteor. Soc. Japan*, **85**, 255−276.

Kawabata, T., T. Kuroda, H. Seko, and K. Saito, 2011: A cloud-resolving 4D-Var assimilation experiment for a local heavy rainfall event in the Tokyo metropolitan area. *Mon. Wea. Rev.*, **139**, 1911−1931.

Mikami, A., T. Kawabata, S. Satoh, J. Furumoto, S. Nagai, Y. Murayama, and T. Tsuda, 2011: Meso-γ-scale convective systems observed by a 443-MHz wind-profiling radar with RASS in the Okinawa subtropical region. *J. Atmos. Sol. Terr. Phys.*, **73**. 996−1009.

Minda, H., F. A. Furuzawa, S. Satoh, and K. Nakamura, 2010: Convective boundary layer above a subtropical island

observed by C-band radar and interpretation using a cloud resolving model. *J. Meteor. Soc. Japan*, **88**, 285–312.

National Imagery and Mapping Agency, 1997: *Department of defense world geodetic system 1984, its definition and relationships with local geodetic systems*. 3rd ed., NIMA Tech. Rep. TR8350.2.

Saito, K., T. Fujita, Y. Yamada, J. Ishida, Y. Kumagai, K. Aranami, S. Ohmori, R. Nagasawa, S. Kumagai, C. Muroi, T. Kato, H. Eito, and Y. Yamazaki, 2006: The operational JMA nonhydrostatic mesoscale model. *Mon. Wea. Rev.*, **134**, 1266–1298.

Shoji, Y., 2009: A study of near real-time water vapor analysis using a nationwide dense GPS network of Japan. *J. Meteor. Soc. Japan*, **87**, 1–18.

Shoji, Y., 2013: Retrieval of water vapor inhomogeneity using the Japanese nationwide GPS array and its potential for prediction of convective precipitation. *J. Meteor. Soc. Japan*, **91**, 43–62.

Shoji, Y., H. Nakamura, T. Iwabuchi, K. Aonashi, H. Seko, K. Mishima, A. Itagaki, R. Ichikawa, and R. Ohtani, 2004: Tsukuba GPS dense net campaign observation: Improvement in GPS analysis of slant path delay by stacking one-way postfit phase residuals. *J. Meteor. Soc. Japan*, **82**, 301–314.

Zou, X., and Y.-H. Kuo, 1996: Rainfall assimilation through an optimal control of initial and boundary conditions in a limited-area mesoscale model. *Mon. Wea. Rev.*, **124**, 2859–2882.